Application of the up-down separation using PZ calibration filter based on critically refracted waves

Ettore Biondi and Stewart A. Levin

ABSTRACT

On marine multicomponent data we may apply PZ summation to separate the up-going and down-going wavefields. We show an example of this procedure for an ocean bottom nodal (OBN) dataset, where we perform an acoustic decomposition that gives the up- and down-going pressure fields in the water. To design the necessary calibration filters, we target long-offset refracted waves that contain purely up-going energy. After the acoustic separation, we adaptively subtract the down-going wavefield from the original pressure component. The quality of the separation achieved demonstrates that the calibration filters obtained from the long-offset waveforms were effective in decomposing almost all the events present in each gather.

INTRODUCTION

When dealing with multicomponent ocean bottom acquisition (OBN), where both the particle velocity vector and pressure are measured, a fundamental preprocessing step is wavefield up-down separation. In the context of wavefield separation of ocean bottom data, there are two possibilities (Schalkwijk et al., 1999). If we perform an acoustic decomposition, we obtain the down-going pressure just above the ocean bottom, and the up-going pressure just beneath the ocean bottom surface. Alternatively, with an elastic decomposition, we separate the up-going and down-going P- and S-waves just beneath the ocean bottom.

After such wavefield decomposition of the OBN data, the result can be used in further processing. For instance, source signatures can be estimated from the down-going wavefield after source static corrections are applied (Wong and Ronen, 2009). It is also possible to apply up-over-down deconvolution to attenuate all free-surface multiple (Grion, 2010). Furthermore, having a decomposed pressure wavefield leads to a better mirror imaging or a joint least-square inversion of up- and down-going signals (Grion et al., 2007; Wong et al., 2010). These examples are only few applications where we need the decomposition of the wavefield, underscoring the importance of doing this processing step when dealing with ocean bottom acquisition.

There are many different published methods for performing PZ summation (Sonneland et al., 1986; Barr and Sanders, 1989; Amundsen, 1993). In our application, we

proceed with an acoustic decomposition of the pressure field performed in the physical (t-x) domain of an OBN acquisition. Usually, there are differences in coupling and instrument response of the measuring devices. Therefore, the data must be properly calibrated before the pressure (P) and the vertical velocity (Z) components can be combined. We follow the PZ summation algorithm developed by Melbø et al. (2002) where the necessary calibration filter is computed by minimizing the energy of the resulting down-going wavefield within a manually picked window tracking critically refracted waves. We start showing the result of the elimination of the instrument response of both the pressure and vertical velocity components. Then, we explain how the PZ summation algorithm works, and show the results. Finally, we present the result of the adaptive subtraction procedure developed by Alvarez and Guitton (2007) subtracting the down-going pressure obtained from the PZ summation method to the original P component. We applied the acoustic decomposition to all the receivers of the line. Here, we report the result of a representative common-receiver gather belonging to the inner portion of the recording line. Our result demonstrates that the calibration filter based on the long-offset refracted arrivals can be used to separate the energy for all the offset range.

RECEIVER IMPULSE RESPONSE DESIGNATURE

The OBN dataset was recorded in the North Sea and appears in our data library under the name Moere Vest. We worked with a 2D survey composed of 179 multicomponent receivers with a minimum receiver interval of approximately 250 meters (m) and a maximum of 10 kilometers (km). The source interval was approximately 100 m. The inner portion of the line has the fine receiver interval; only at the two ends does the increase to approximately 10 km (see Alves (2014) for all the dataset details).

Figure 1 shows the P and Z components of the representative common-receiver gather, bandpassed to the frequencies contained in the sources. In this figure, you can clearly see the direct arrival and its free-surface multiples, indicated by the green arrows, with periodicity of approximately 2 seconds (s). On this dataset, a debubbling procedure has not been applied and source reverberations are evident. Thanks to the available long offsets, it is possible to observe refracted waves starting at approximately 8 km offset. It is interesting to note the sea-surface multiple of the first refracted arrival centered around 7.5 s on the right side of both components. In addition to these events, a clear primary reflection appears at 2.5 s (pointed by the red arrow). All these events help us understand the result of the wavefield decomposition because they can be easily divided between up- or down-going arrivals. Both components contain the same events except for some water reverberations and shear-wave induced events present in the recorded vertical velocity. However, the different instrument responses cause the equivalent arrivals in the two components to have amplitude and phase differences (compare the direct arrival and its first multiple or the primary reflection at 2.5 s). To compensate for these differences, it is necessary to correct for the different impulse responses of the measuring devices.

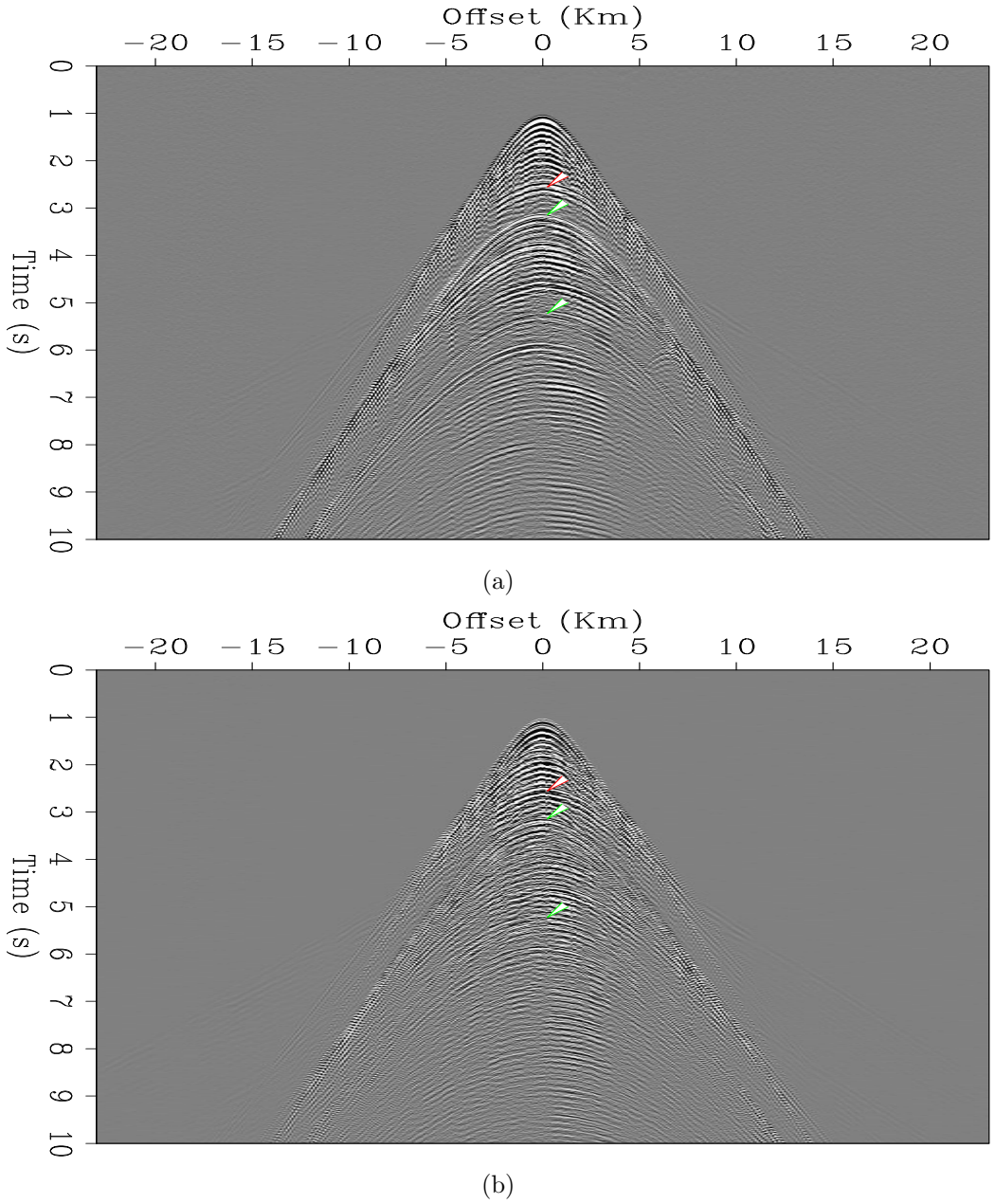

Figure 1: Portion of a common-receiver gather of the Moere Vest OBN dataset. (a) Pressure component of the data. (b) Recorded vertical velocity. In both components there are visible free-surface multiples of the direct arrival with a periodicity of approximately 2 s (indicated by the green arrows). Focusing attention on the near-offset events, it is possible to see one primary reflections centered around 2.5 s (indicated by the red arrow). As expected, the vertical component contains the same events as the recorded pressure, except for a very low energy water reverberations and shear-wave induced noise. However, looking at the gathers carefully, it is possible to see amplitude and phase differences between equivalent arrivals in the two components. This effect is caused by the different instrument response and coupling of the measuring devices. [**ER**]

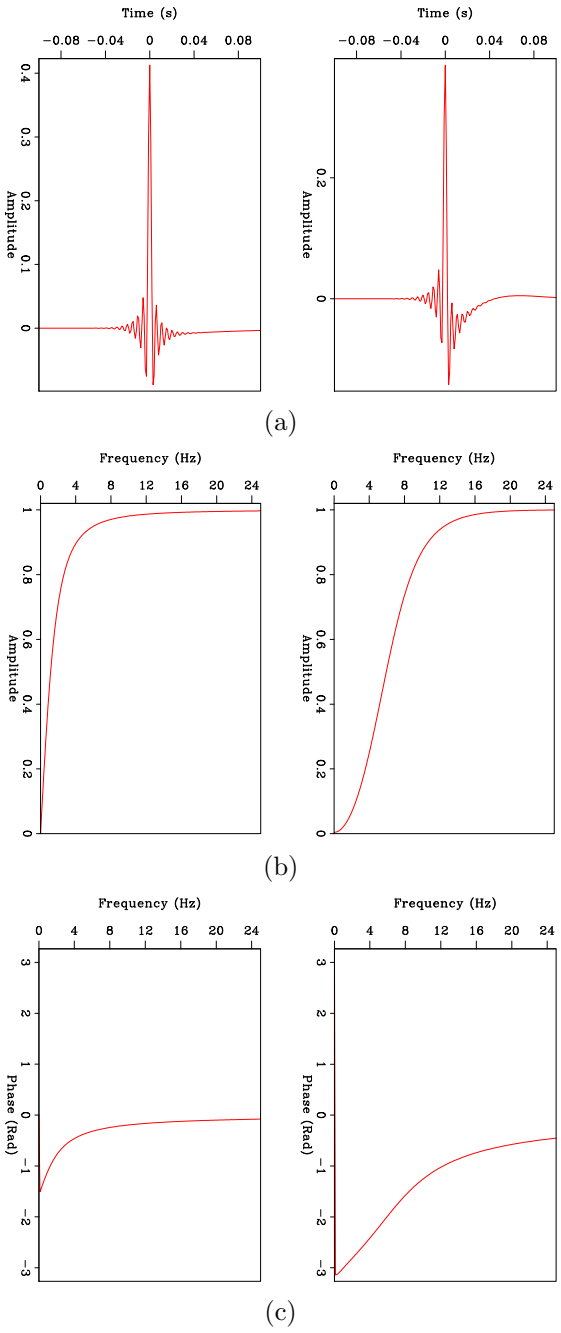

Figure 2: Comparison of the instrument responses of the hydrophone (right panels) and of the geophone (left panels). (a) Instrument responses in the time domain. (b) Amplitude spectra of the responses of the measuring devices. (c) Phase spectra of the instrument responses. It is interesting to point out the noncausality of both instrument responses. This nonphysical feature is present because the data has been previously corrected for the linear phase shift of the antialiasing filter (approximately 60 ms), and it has been taken into account in the computed instrument responses. [**ER**]

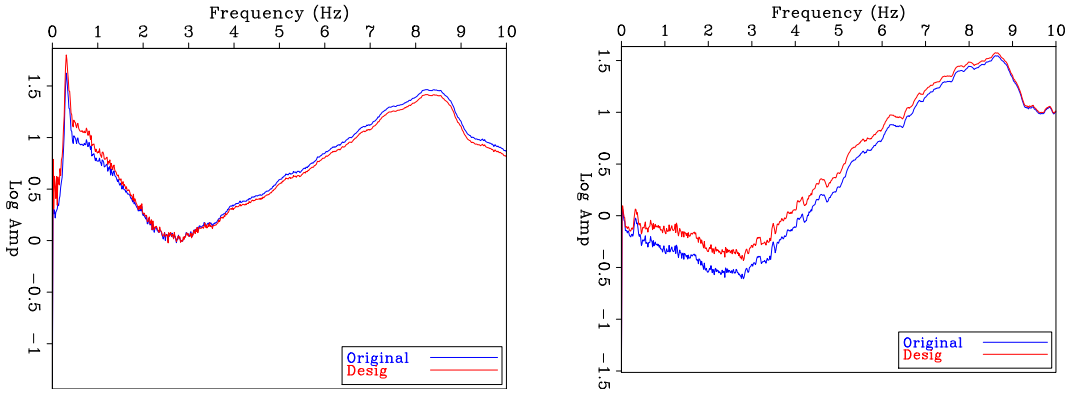

Figure 3: Comparison between the amplitude spectra of the pressure (a) and vertical (b) components before and after the instrument impulse response designature. The receiver designature boosts the low frequencies in both the components of the data. [**ER**]

Fortunately, we were provided with impulse responses of the deployed hydrophone and geophone. Figure 2a displays the time impulse responses for the hydrophone and the geophone, on the right and left respectively. One curious feature of these responses is their noncausality, which is caused by the correction for the linear phase shift introduced by the the antialiasing filter during the recording of the data. Looking at the amplitude spectra responses (Figure 2b), we see that the effect of the receiver impulse response designature boosts the low frequencies for both components. Regarding the phase instrument spectra, shown in Figure 2c, it is possible to see that the phase correction for the geophone affects wavelet shapes more then the correction for the hydrophone. Figure 3 shows the comparison of the amplitude spectra before and after the receiver impulse response correction for both components. In the case of the hydrophone, the frequencies up to 4 Hertz (Hz) have been noticeably boosted; while for the geophone, the correction has enhanced frequencies up to approximately 9 Hz.

Comparing equivalent events present in both the components of the representative common-receiver gather after the receiver response designature, affirms that indeed, this preprocessing procedure eliminated most of the amplitude and phase differences between the recorded P and Z (Figure 4). Now, the P and Z components behave according to what theory predicts: the direct arrival and free-surface multiples in the pressure have opposite polarity respect the same events in the Z component. Instead, the refracted first breaks and primary reflections have the same polarity on the two components (e.g., the reflection centered at 2.5 s).

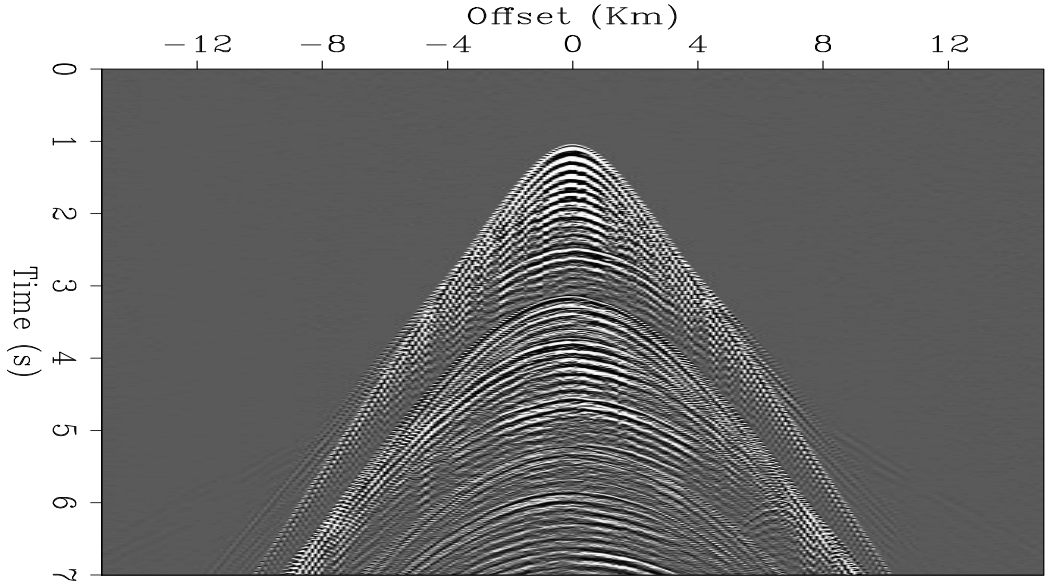

(a)

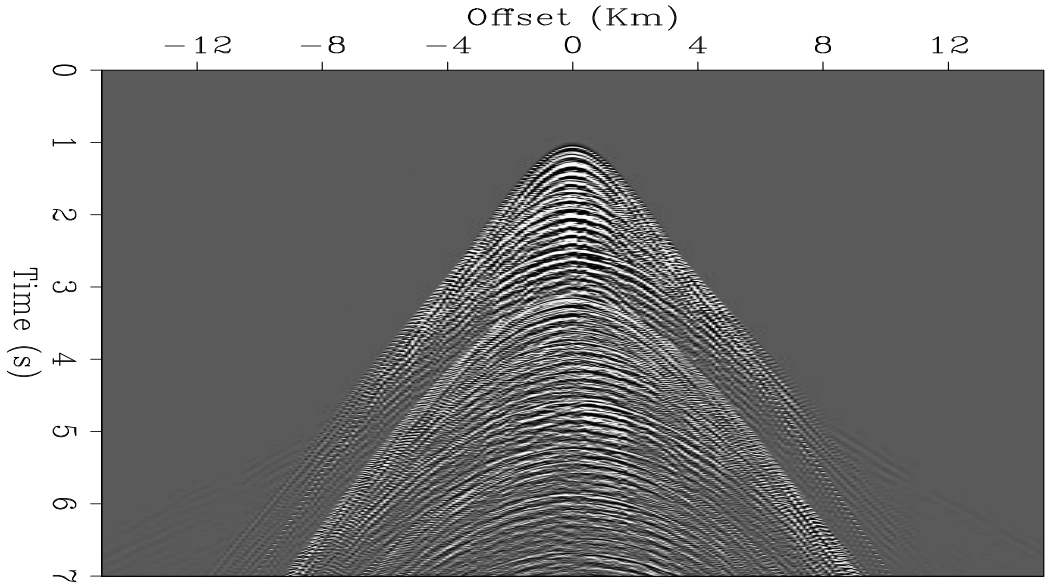

(b)

Figure 4: Close-ups the common-receiver of Figure 1 after the the receiver response designature. The correction for the different responses of the instruments makes the up-going events (e.g., refracted and diving waves) in the pressure (a) and the vertical (b) components more similar, and down-going events (e.g., the direct arrival and free-surface multiples) to have the opposite polarity. [**ER**]

UP-DOWN SEPARATION THROUGH PZ SUMMATION

Having compensated for the different instrumental impulse responses, we now have to correct the data for the coupling effect that still affects our data. This correction is conducted by means of a calibration filter $a(f)$ applied to one of the two recorded components, which in our case, is the vertical velocity. Using this filter for performing the acoustic decomposition, the up- and down-going pressure wavefields can be expressed as follows:

$$P_{up}(f,k) = \frac{1}{2}P(f,k) + a(f)\frac{\rho}{2q(f,k)}Z(f,k), \tag{1}$$

and

$$P_{down}(f,k) = \frac{1}{2}P(f,k) - a(f)\frac{\rho}{2q(f,k)}Z(f,k), \tag{2}$$

respectively, where P is the pressure, f is the frequency, k is the horizontal wavenumber, Z is the vertical velocity component, ρ is the density of the water, and q is the vertical slowness in the water layer. This last factor is related to the ray parameter p with the following relation:

$$q(f,k) = \sqrt{c^{-2} - p^2(f,k)}, \tag{3}$$

where c is the velocity of the water at the receiver position. These equations hold for common-shot gathers, but it is possible to use them for decomposing wavefields in common-receiver gathers (Schalkwijk et al., 1999). The calibration filter $a(f)$ is found by minimizing the energy of the down-going pressure (Eq. [2]), in a least-squares sense, in a window containing only up-going events.

In our application, we manually picked a window tracking refracted waves before the first refracted multiple events. In particular, we picked a window of approximately 1 s of the long-offset refracted waves between 11 km and 15 km. To find the calibration filter, we computed a Wiener shaping filter that shapes the Z component wavelets to the wavelets of the pressure wavefield within the picked window. As a result, such a filter also incorporates the density and slowness factors of Equations (1) and (2). The density factor does not vary for all the receiver gather. Instead, the vertical slowness varies both in frequency and wave-number (or time and offset in the physical domain). Inside the window, we can assume that the slowness factor to be constant, and we can easily compute it using the slope of the first break refracted arrivals. To simplify the computation of the varying vertical slowness in the rest of the gather, we

calculated the local slowness of the events inside the gather using a constant water velocity model with the vertex of the first hyperbola centered at the apex time of the direct arrival. Above the direct arrival, we use the slope of the refracted waves for all the other events. In addition, the vertical slowness is considered to be local, and such assumption allows us to use it as a multiplicative factor in the physical domain. Without this assumption, it would be a bidimensional convolution in the offset-time domain.

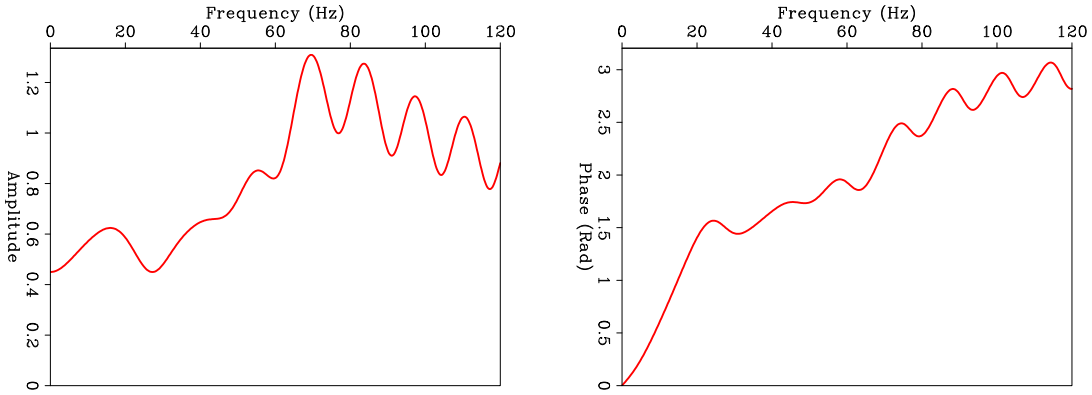

(a) (b)

Figure 5: Frequency response of the calibration filter with 41 coefficients obtained from the long-offset refracted waves. (a) Amplitude spectra of the filter. (b) Phase spectra of the filter. [**ER**]

Figure 5 shows a plot of the amplitude and phase frequency response of the calibration filter with 41 coefficients. The plot clearly shows that the filter varies with frequency. Therefore, the coupling differences between the two components are not related to a simple scalar amplitude factor. In fact, the result obtained only with a constant calibration factor in Melbø et al. (2002) demonstrated the limitations of such white spectra filter.

In Figure 6, we display the result of the PZ algorithm after calibrating the Z component of the reported receiver with the filter of Figure 5. In the down-going wavefield, most of the up-going energy has been attenuated; indeed, the primary reflection at 2.5 s has almost completely vanished. Furthermore, the primary refracted events are separated and present in the up-going pressure wavefield; whereas, the free-surface multiples of the critically refracted waves are present only in the down-going component. In the up-going pressure, it is now possible to identify two distinct primary reflections, one at 1.9 s and the other at 2.5 s. The leftover down-going energy still present in the up-going wavefield is cause by the fact that we performed an acoustic separation where we are obtaining the up-going pressure just beneath the sea bottom (Grion, 2010).

To improve the result for the up-going wavefield, and, therefore decrease the leakage of down-going energy into it, we adaptively subtract the down-going pressure of Figure 6b from the original P component of Figure 1a. The adaptive subtraction

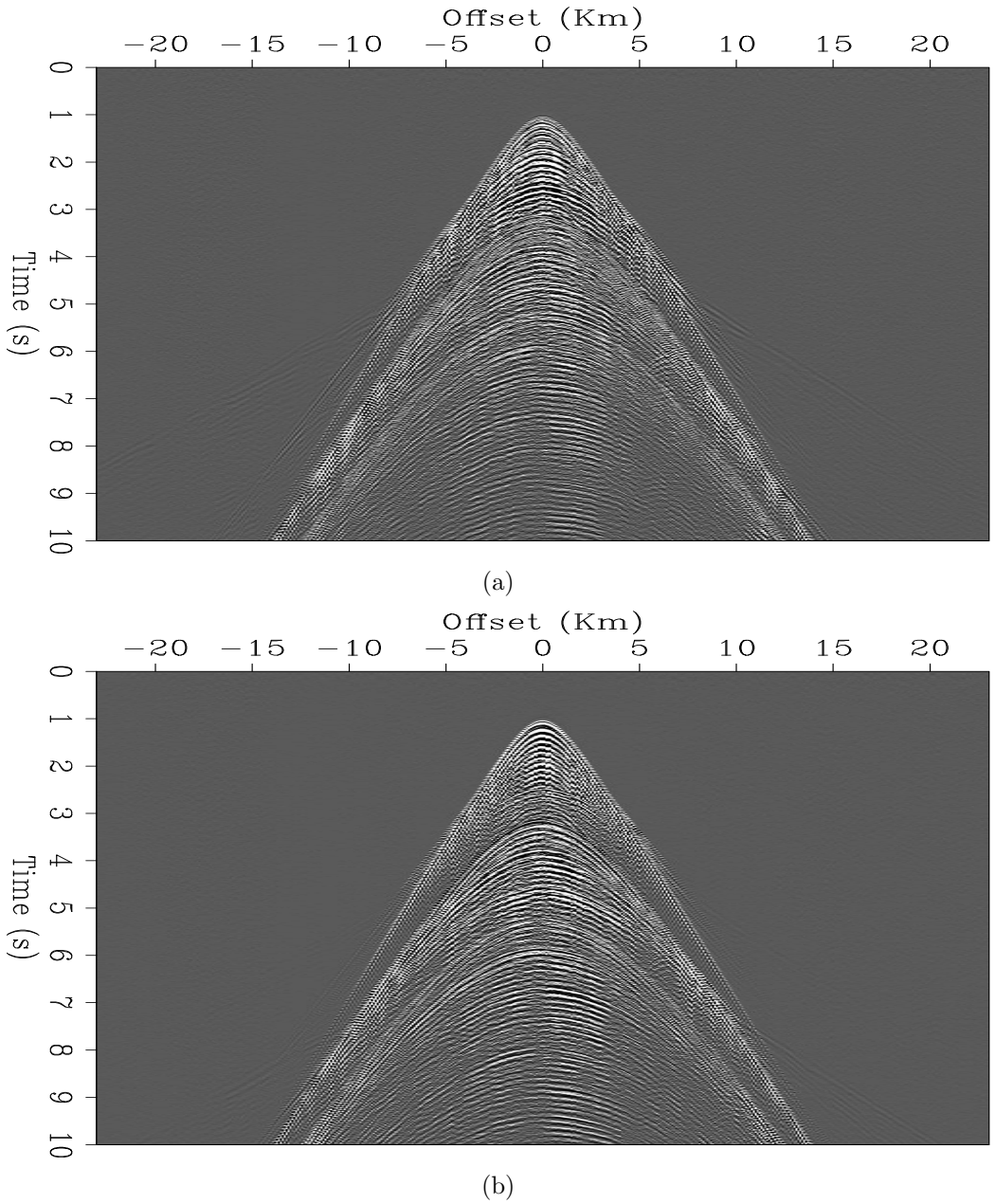

Figure 6: Output of the PZ summation having applied the calibration filter of Figure 5 to the vertical component. (a) Up-going pressure wavefield just beneath the ocean bottom. (b) Down-going just above the ocean bottom. Most of the energy is well separated, especially for the down-going wavefield where most of up-going refracted arrivals are attenuated. Note that the multiple of these events are present only in the down-going pressure. Because we are performing an acoustic decomposition, some of the energy of the down-going waves is still present in the up-going wavefield. Despite that, the two primary reflections centered about 1.9 s and 2.5 s are only present in the up-going pressure. [**ER**]

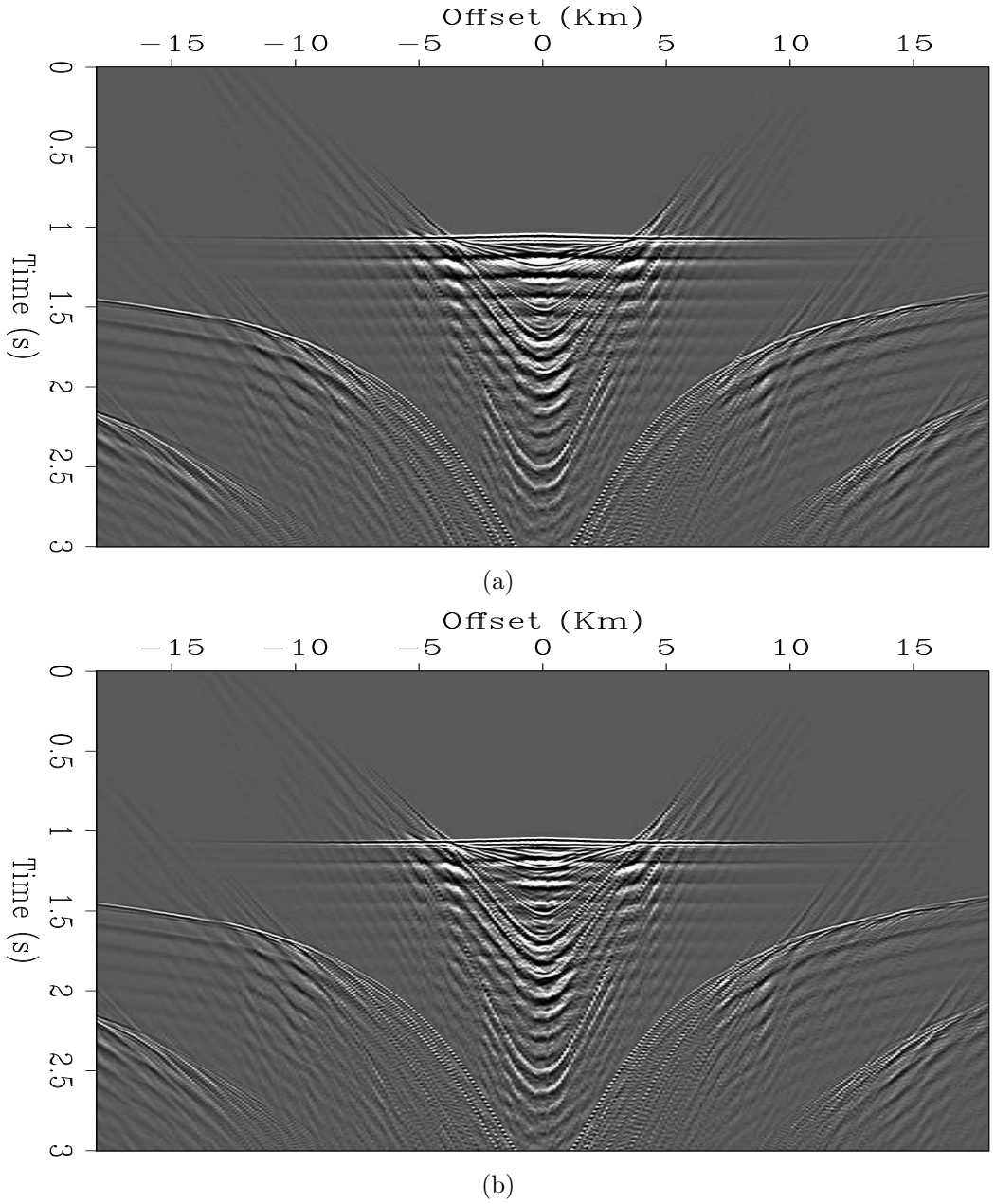

Figure 7: Result of the adaptive subtraction of the down-going wavefield of Figure 6b from the pressure component of Figure 4a after the hyperbolic moveout (HMO) correction with a water velocity of 1,475 m/s. (a) Close-up of Figure 6a after the HMO correction. (b) Resulting up-going pressure using the adaptive subtraction developed by Alvarez and Guitton (2007). In the up-going wavefield obtained with the adaptive subtraction routine, the direct arrival and its bubble is clearly attenuated. [**ER**]

was conducted with the algorithm developed by Alvarez and Guitton (2007) using a five-coefficient temporal matching filter applied to all the data in the gather. Comparing the up-going pressure obtained with the PZ algorithm with the same wavefield conducted using the adaptive subtraction (Figure 7), after performing the hyperbolic moveout (HMO) correction with water velocity, it is clearly visible that the adaptive subtraction routine further attenuated the direct arrival and its bubble pulses.

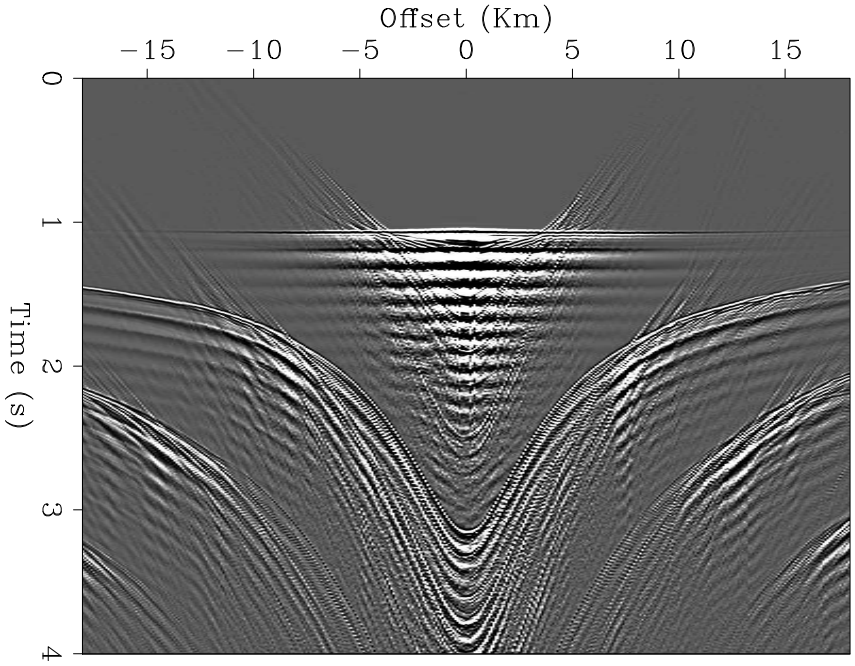

Figure 8: Close-up of the down-going pressure of Figure 6b after the application of the HMO correction. Looking at the direct arrival, it is possible to see 12 pulses of the source on the near offsets. The leakeage of up-going energy (e.g. refractions at about 4 km offset) it is caused by the simple slowness model and the local approximation considered in the PZ summation algorithm. [**ER**]

It is interesting to see the down-going pressure wavefield after applying the HMO correction with water velocity (Figure 8). The direct arrival and its bubble become flat and easily detectable. Although some energy of the primary events leaks into this wavefield, because of the simple slowness model and the local approximation used, it is possible to distinguish up to 12 pulses of the source. This wavefield is indeed a point of departure for the source estimation and further processing, such as the debubbling of the data.

To evaluate the quality of the wavefield separation for the other receivers, in Figure 9 we show the costant-offset section at approximately 0 km offset. In the up-going pressure field section, obtained with the adaptive subtraction algorithm, the direct arrival and its reverberations are attenuated for all the shown receivers. The two primary reflections previously highlighted are evident and it is possible to follow their trend along the acquisition line. In addition, in the down-going wavefield section

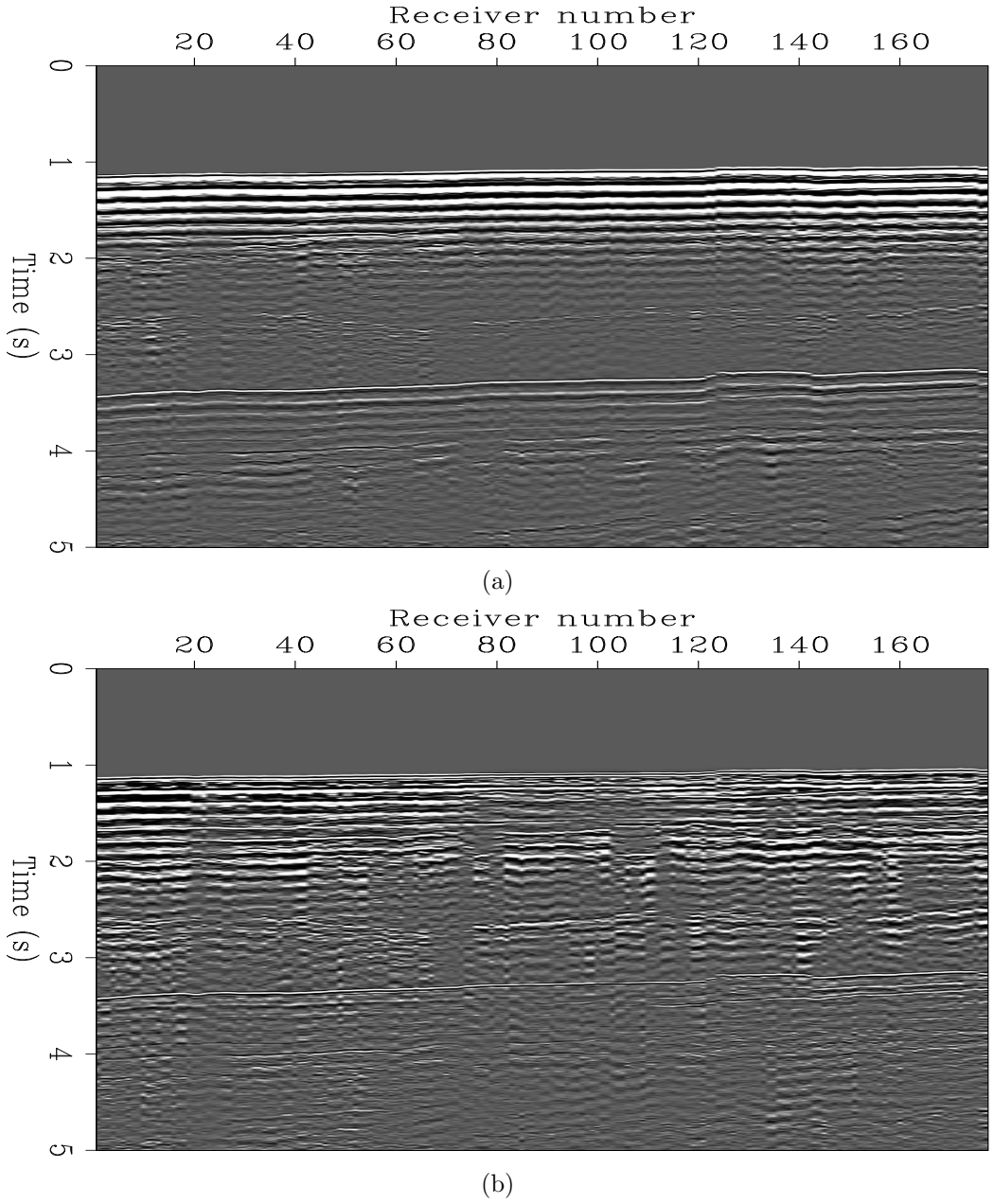

Figure 9: Comparison between constant-offset sections for the up- and down-going wavefields at approximately zero offset. (a) Constant-offset section of the down-going pressure field. (b) Constant-offset section of the up-going wavefield obtained with the adaptive subtraction. In the top panel, the two events around 1.9 and 2.5 are primary reflections. It is possible to see their trend along the acquisition line. Instead, in the bottom panel the direct arrival and its first free-surface multiple are clearly visible. In addition, in this section are present the two first multiples of the mentioned primary reflections. [**CR**]

the free-surface multiples of the two reflections are visible, albeit they have a lower amplitude.

CONCLUSIONS

We performed an acoustic decomposition of the wavefield of OBN data using a PZ summation algorithm based on calibration filters computed from the critically refracted waves. To compensate for the different impulse responses and coupling of the recording devices, we first proceeded with an instrument response designature for both the components. After that, we picked a window containing only up-going refracted waves and design a shaping filters necessary for the calibration of the recorded vertical velocity. After performing the PZ summation step, having separated the pressure into up- and down-going energy, we improved the result of the up-going wavefield by employing an adaptive subtraction scheme. Our result demonstrates that the designed calibration filters were effective in decomposing almost all the events for all the offsets. In addition, the up-going wavefield obtained through the adaptive subtraction is less contaminated by the leakage of the down-going energy respect the same wavefield conducted using only the PZ summation algorithm. These two decomposed pressure fields enabled us to performing further processing, such as source signature estimation and debubbling.

ACKNOWLEDGMENTS

We thank Seabed Geosolutions for releasing the field data and for supporting the data handover by Paul Miligan and Shuki Ronen.

REFERENCES

Alvarez, G. and A. Guitton, 2007, Simultaneous adaptive matching of primaries and multiples with non-stationary filters: SEP-Report, **125**, 61–77.

Alves, G., 2014, Overview of the Moere Vest data set: SEP-Report, **155**.

Amundsen, L., 1993, Wavenumber-based filtering of marine point-source data: Geophysics, **58**, 1335–1348.

Barr, F. J. and J. L. Sanders, 1989, Attenuation of water-column reverations using pressure and velocity detectors in a water-bottom cable: SEG Expanded Abstracts, **59**, 653–656.

Grion, S., 2010, From PZ sum to wavefield separation, mirror imaging and up down deconvolution: The evolution of OBS data processing: KazGeo 2010, 83–87, European Association of Geoscientists and Engineers.

Grion, S., R. Exley, M. Manin, X. Miao, A. L. Pica, Y. Wang, P. Granger, and S. Ronen, 2007, Mirror imaging of OBS data: First Break, **25**, 37–42.

Melbø A. H. S., J. O. A. Robertsson, and D. Manen, 2002, PZ calibration by applying the equation of motion to critically refracted waves, 1030–1033. Soc. of Expl. Geophys.

Schalkwijk, K. M., C. P. A. Wapenaar, and D. J. Verschuur, 1999, Application of two-step decomposition to multicomponent ocean-bottom data: Theory and case study: Journal of Seismic Exploration, **8**, 261–278.

Sonneland, L., L. E. Berg, P. Eidsvig, A. Haugen, B. Fotland, and J. Vestby, 1986, 2-d deghosting using vertical receiver arrays: SEG Expanded Abstracts, **5**, 516.

Wong, M., B. Biondi, and S. Ronen, 2010, Joint least-squares inversion of up- and down-going signal for ocean bottom data sets: SEP-Report, **140**, 83–94.

Wong, M. and S. Ronen, 2009, Source signature and static shifts estimations for multi-component ocean bottom data: SEP-Report, **138**, 223–32.